



Role of zirconia nanoparticles on microstructure, excess conductivity and pinning mechanism of BSCCO superconductor ceramics

M. Zouaoui¹ · M. Ben Salem¹ · Y. Slimani² · H. S. Aldosari³ · F. Ben Azzouz^{3,4}

Received: 24 February 2023 / Accepted: 18 June 2023 / Published online: 24 June 2023
© The Author(s), under exclusive licence to Springer-Verlag GmbH, DE part of Springer Nature 2023

Abstract

Using the solid-state reaction process, we prepared $(\text{Bi,Pb})_2\text{Sr}_2\text{Ca}_2\text{Cu}_3\text{O}_{10-\delta}$ (Bi-2223 for brevity) ceramics with the addition of zirconium dioxide (ZrO_2) nanoparticles. The proportion x of ZrO_2 per the total masse of superconductor ranged from 0 wt.% to 0.2 wt.%. We report the intragrain critical current density (J_c), pinning mechanisms, and thermal fluctuations induced excess conductivity. Employing numerous characterization techniques, combining X-rays diffraction, electrical transport measurements, scanning and transmission electron microscopes (SEM and TEM), and DC magnetization hysteresis measurements, we find that the ceramic sintered with 0.1 wt.% ZrO_2 nanoparticle showed the best superconducting performance. From the analysis of excess conductivity using Aslamazov–Larkin model, we assessed the crossover temperatures between different regimes of conductivity, the penetration depth, the coherence length, as well as the upper and the lower critical magnetic fields (B_{c1} , B_{c2}) at zero kelvin for all the ceramics. Critical current density versus temperature deduced from magnetization measurement is raised by NP- ZrO_2 addition. Thereby, NP- ZrO_2 strengthened the role of δl pinning cores and enhanced the flux pinning ability.

Keywords $\text{YBa}_2\text{Cu}_3\text{O}_{7-\delta}$ superconductor · Microstructure · Electrical properties · Excess conductivity · Magnetic properties · Pinning mechanisms

1 Introduction

Because of their prospective applications, high-temperature superconductors (HTS) have gathered great interest [1, 2]. Among HTS materials, $\text{Bi}_2\text{Sr}_2\text{Ca}_{n-1}\text{Cu}_n\text{O}_{2n+4-\delta}$ is

considered as a unique system, which possesses three compounds Bi-2201, Bi-2212, and Bi-2223 with critical transition temperature (T_c) of 10 K, 90 K, and 110 K, respectively. Bi-2223 owns some benefits including high T_c , high density of critical current (J_c) and magnetic field-carrying capability, leaving this compound the most significant in applications. However, Bi-2223 compound presents disadvantages such as brittle linkages between grains and frail capability of magnetic flux pinning (FP) that restricts their exploitation as superconductors in potential applications. Moreover, due to its reduced thermodynamic stability domain and the complex mechanism of its formation, the production of pure Bi-2223 compound is a hard job and Bi-2201 and Bi-2212 phases cannot be avoided during the growth of Bi-2223.

Lead addition to the BSCCO system is considered as a hopeful strategy for enhancing the stability and purity of the Bi-2223 compound [3, 4]. The Bi-2223 polycrystalline superconducting traits at zero as well as under an external magnetic field are closely allied with the level of crystal defects inside the product and the weak link between grains. Chemical substitution and addition processes are broadly used to remedy the limitations of J_c and fulfill the

✉ Y. Slimani
yaslimani@iau.edu.sa; slimaniyassine18@gmail.com

✉ F. Ben Azzouz
Fkazzouz@iau.edu.sa

¹ Laboratory of Physics of Materials: Structure and Properties LR01ES15, Faculty of Science of Bizerte, University of Carthage, Zarzouna, 7021 Bizerte, Tunisia

² Department of Biophysics, Institute for Research and Medical Consultations (IRMC), Imam Abdulrahman Bin Faisal University, P.O. Box 1982, Dammam 31441, Saudi Arabia

³ Department of Physics, College of Science, Imam Abdulrahman Bin Faisal University, P.O. Box 1982, Dammam 31441, Saudi Arabia

⁴ Basic and Applied Scientific Research Center, Imam Abdulrahman Bin Faisal University, P.O. Box 1982, Dammam 31441, Saudi Arabia

requirements of better FP capacity. The convenient density of flux pinning cores (FPC) with strong pinning ability are vital factors that decide the values of critical parameters J_c and H_c . Effective FPC related to crystal defects, like lattice strains, structural inhomogeneities, and non-superconductive phase inclusions, depend on the synthesis process, on the doping contents and types, and on the kind of atoms that could substitute the distinct position in Bi-2223. Massive efforts have been performed to optimize proceedings that enable the production of Bi-2223 polycrystalline materials with convenient T_c , J_c and H_c and best FP [5–8]. Some chemical inclusions lead jointly to the deterioration of intergranular properties and intensification of intragranular properties [9–12]. For example, Bi₂Te₃ nanoparticles added as a foreign phase in Bi-2223 settle in intragrain and intergrain regions to harm the crystallinity and reduce the electrical properties [9]. However, encouraging effects of many nano-oxide entities addition on J_c , B_{c2} , and pinning properties have been identified [13–21]. The inclusion of a small concentration (0.2 wt.%) of TiO₂ nanorods improves J_c by 64% roughly [11]. Oztürk et al. [21] revealed that addition of 0.1 wt. % of carbon-encapsulated nano boron enhances the volume fraction of Bi-2223 to 79.87% and rises the J_c at a temperature of 10 K by a factor of about three times. Jannah et al. [13] worked on Ag-sheathed Bi-2223 superconducting tapes with the addition of Co₃O₄ nanoparticles and showed that the value of J_c of 0.02 wt % Co₃O₄ (30 nm) added sample is more than six times compared to the non-added one.

Whatever the defects generated naturally or artificially inside the HTS system, they stimulate the thermal fluctuations of the superconducting order parameter above T_c . These fluctuations induce an excess of conductivity $\Delta\sigma$. Owing to elevated T_c , small coherence length, and large anisotropy, the behavior of fluctuation-induced conductivity (FIC) is largely amplified in the HTS. Many researchers extended the study of Bi-2223 compound by exploring the experimental data of FIC to discuss the dimensionality of conductivity and determine the crossover temperatures, the coherence length, the interlayer coupling, the inter-plane spacing, and critical physical parameters at zero Kelvin, as upper and the lower critical magnetic fields ($B_{c1}(0)$, $B_{c2}(0)$) and critical current density $J_c(0)$ [22–28]. Some studies were devoted to the impact of nano-oxide, and few stressed the non-oxide nano-entities. Aftabi et al. [22] examined the FIC of (Bi_{1.6}Pb_{0.4})Sr₂Ca₂Cu₃O_{10+ δ} superconductor added with ZnO nanoparticles and they conclude that when the ZnO NPs content increases up to 0.3 wt. % the width of the 3D regime of fluctuations is narrowed but that of 2D is augmented. ZnO NPs nanoparticles proved their ability to enhance $B_{c1}(0)$, $B_{c2}(0)$ and $J_c(0)$ and the best are obtained for 0.2 wt. % ZnO NPs addition. The inclusion of nano-NiO up to 0.05 wt.% in (Bi,Pb)-2223 yields an increase in ξ_{co} and d [25]. Habanjar et al. [26] analyzed the FIC of (BaSnO₃) _{x} (Bi_{1.6}Pb_{0.4})Sr₂Ca₂Cu₃O_{10- δ} samples and

demonstrated that the parameters ξ_{co} and d were reduced by increasing the concentration of nano-BaSnO₃ up to 0.5%, then increased with further addition. Roumié et al. [27] worked on (nano-Fe₂O₃) _{x} /Bi_{1.8}Pb_{0.4}Sr₂Ca₂Cu₃O_{10+ δ} samples where x varies from 0 to 1.5 wt. %. They confirmed that nano-Fe₂O₃ increased the parameters ξ_{co} , J and d , and worsened $B_{c1}(0)$, $B_{c2}(0)$ and $J_c(0)$. Loudhaief et al. [23, 28] focused on the effect of the CuS, (Cu_{0.99},Eu_{0.01})S and (Cu_{0.99},La_{0.01})S nano-materials addition in Bi-2223. They analyzed the FIC by five fluctuations regions and reported variations in ξ_{co} and d . The 0.2 wt% of nano-(Cu_{0.99},La_{0.01})S proves their capability to strengthen $B_{c2}(0)$ value from 271 to 896 T, however a little increase of $J_c(0)$ was recorded.

In the present report, we aim to investigate the effect of Zirconium dioxide (ZrO₂) nanoparticles (NPs) on the superconducting properties of Pb-doped Bi-2223. The strong interest in ZrO₂ particles stems from their attractive physical properties and their promising applications. NPs of ZrO₂ have special properties such as high thermal stability, low thermal conductivity at high temperatures, quite high thermal expansion coefficient, good ionic conductivity, and high mechanical strength. These properties have led to the utilization of ZrO₂ nanoparticles in a wide range of industrial applications including oxygen sensors, fuel cells, catalysts, solid electrolytes, and the fabrication of dense ceramics [29–32]. ZrO₂-NPs is an attractive additive in BSCCO superconductors because its melting temperature of ~2715 °C is so high as compared to the sintering temperature of Bi-2223 (~835 °C). ZrO₂ is chemically inactive, and its presence cannot hamper the Bi-2223 phase formation. Hence, ZrO₂ could be desirable criterion to make superconductor composites with promising physical properties. Moreover, it has been reported that ZrO₂-NPs included in HTS systems work as effective FPC and enhance the critical current densities [33, 34]. The J_c values under a low applied magnetic field of ZrO₂-added Bi-2223 were performed via magneto-resistivity measurements and it was found that the grain boundaries are heightened and the J_c is upgraded with the addition of 0.1wt% ZrO₂ [35]. In this study, the dependence of x wt% NPs ZrO₂ ($x=0.0, 0.1, \text{ and } 0.2$) addition on the FIC of the BSCCO system prepared by a three-stage solid-state reaction route was described. It is intended to determine some important superconducting parameters at a temperature of 0 K, as $J_c(0)$, $B_{c1}(0)$ and $B_{c2}(0)$, and survey the relationship between the FIC above T_{co} and the pinning mechanisms displayed in the superconducting state. Thereby, the pinning mechanisms are estimated through DC magnetic measurements at various operating temperatures from 10 to 77 K.

2 Experimental details

Bi₂Sr₂Ca₂Cu₃O_{10- δ} bulk ceramics fortified by ZrO₂ nanoparticles with an average size of about 20 nm were synthesized via the solid-state reaction process. The heat

treatment process was made in crucibles of alumina. First, stoichiometric amounts of high-purity (99.9%) raw reactants of strontium carbonate (SrCO₃), calcium carbonate (CaCO₃), and oxides of copper (CuO), filling the chemical composition Sr_{1.9}Ca_{2.1}Cu₃O₈, were crushed and calcinated in the air at 920 °C during 48 h. Next, we added to the beforehand obtained precursor bismuth oxide (Bi₂O₃) and lead oxide to fulfill the composition Bi_{1.6}Pb_{0.4}Sr_{1.9}Ca_{2.1}Cu₃O_{10-d}. The mixture was crushed, compacted, and then sintered at 835 °C for 144 h in air. The Bi_{1.6}Pb_{0.4}Sr_{1.9}Ca_{2.1}Cu₃O_{10-d} powders resulting from pellets obtained in the previous stage were reground with 5 wt.% PbO and *x*% of ZrO₂ nanoparticles (*x* = 0 wt.%, 0.1 wt.%, 0.2 wt.% per the total mass of superconductor), pressed into pellets with a diameter of 13 mm under 12 tons, sintered at 835 °C for 72 h in air and then finally cooled slowly to room temperature. The amounts of ZrO₂ were selected based on a previous report [29], which reveals that the optimal values of *J_c* measured at 77 K are achieved for ZrO₂ concentration close to 0.1wt.%. In the rest of the text, we mention samples as B-0.0, B-0.1 and B-0.2 in accordance with the concentration *x* = 0 wt.%, 0.1 wt.%, 0.2 wt.% ZrO₂ respectively.

X-ray powder diffraction (Bruker D8, XRD) with CuKα radiation is used for crystal structure examination and quantitative analyses of mixtures of solid phases. The data were recorded in the range of 2θ = 2°–50° by steps width of 0.02°. A scanning electron microscope (SEM, JEOL JEM-5510) was used for the morphological observations. FEI Tecnai G2 TEM coupled with an EDX system was utilized to examine the microstructure and the chemical composition. To estimate *J_c*, DC magnetization versus magnetic field measurements were performed at temperatures varying from 10 to 77 K using a SQUID magnetometer (PPMS-7) with a maximum field of 7 T, with an applied field *H_a*, growing from zero to an extreme value of 60 kOe, then falling to zero, reversing in sign to an extremely negative value of 60 kOe, and finally growing again to 60 kOe. The temperature dependence of electrical resistivity (*ρ(T)*) was executed from ambient temperature (285 K) to 20 K using the four-probe electrical contact method.

3 Method of excess conductivity analysis

The granular character, anisotropic, low charge carrier density, and short superconducting coherence length of HTS materials predispose them to display a significant broad rounding in the transition region (TR). The deviation from the linear relation between resistivity and temperature in the TR is linked to the fluctuation of the order parameter *ψ* of superconducting carriers. Beyond the

normal-superconductor transition, it is likely that superconducting pairs can have an existence with a finite lifetime. Because of the thermal disequilibrium superconducting pairs are simultaneously created and destroyed as the temperature approaches *T_c*. The creation of the Cooper pairs gives an increase in the excess conductivity (*Δσ*) of the carriers. *Δσ* investigation permits also to extract some important physical critical quantities for a temperature of 0 K, such as *J_c(0)*, *B_{c1}(0)* and *B_{c2}(0)* and to acquire information about the properties of flux trapping of HTS materials. The most simplified method to inspect the FIC as a function of temperature is proposed by Aslamazov-Larkin (A-L) [36]. Nearby the superconducting transition temperature, the excess conductivity is defined as:

$$\Delta\sigma(T) = \rho_m^{-1}(T) - \rho_n^{-1}(T) = A_F t^{\lambda_D},$$

where *ρ_m(T)* is the recorded resistivity during the temperature variation, *ρ_n(T)* is the normal resistivity in which the material has a metallic behavior. The coefficient *A_F* designate the amplitude of conduction, $t = \frac{T}{T_{cmf}} - 1$, where *T_{cmf}* denotes the mean-field temperature and *λ_D* depicts the conduction dimensionality. Closer to *T_{cmf}*, the resistive transition occurs in two stages; a pairing transition happens in small and homogeneous isolated regions at temperatures slightly above *T_{cmf}* (para-conductivity zone) and a coherence transition (para-coherent zone) which takes place in the weak links between the superconducting grains at temperatures lesser than *T_{cmf}*. Value of *λ_D* and the expressions of *A_F* for the three possible regimes of fluctuation of conductivity in the mean-field region (MFR) are regrouped in Table 1. The 3D and 2D regimes of conductivity cross at the Lawrence–Doniach [37] temperature $T_{3D-2D} = T_{cmf} [1 + 4(\xi_{co}/d)^2]$, where $(\xi_{co}/d)^2 = J$ denoted the coupling factor between adjacent planes. MFR is embraced at low temperatures by a critical (Cr) fluctuation regime with exponent $\lambda_{1cr} = -2/3$ for two and $\lambda_{2cr} = -1/3$ for three dimensions conductivity, and at high temperature by a short-wave (SW) fluctuation regime with exponent $\lambda_{SW} \sim -3$. At temperature *T_G*, a transition from critical to 3D fluctuation regimes will take place. For 0 K, the anisotropy factor, *γ*, and the thermodynamic critical field, *B_{co}*, are allied to *T_G* (Ginsburg temperature)

Table 1 *λ_D* and *A_F* for the three possible conduction dimensionalities

Conductivity dimensionality	<i>λ_D</i>	<i>A_F</i>
3D	− 0.5	$e^2 / (32\hbar\xi_{co})$
2D	− 1.0	$e^2 / (16\hbar d)$
1D	− 1.5	$e^2 \xi_{co} / (32\hbar s)$

e is the electric charge, *ħ* is the Planck constant, *s* is the cross-sectional area of the 1D wire system, *d* is the effective thickness of the 2D layer system and *ξ_{co}* the coherence length along the *c*-axis for 0 K

as $| (T_G/T_c) - 1 | = \frac{1}{2} [k_B/B_{co} \gamma^2 \xi_{co}^3]^2$, where k_B depicts the Boltzmann constant. The penetration depth λ_o at zero temperature could be evaluated with the help of the expression $B_{co} = \frac{\Phi_o}{2\sqrt{2}\pi\lambda_o\xi_{co}}$, here Φ_o represent the flux quantum number. $B_{c1}(0), B_{c2}(0)$, and $J_c(0)$ will be estimated by using these relations: $B_{c2}(0) = \sqrt{2}\kappa B_{co}$, $B_{c1}(0) = \frac{B_{co}}{\kappa\sqrt{2}} \ln\kappa$ and $J_c(0) = \frac{4\kappa B_{c1}}{3\sqrt{3}\lambda_o \ln\kappa}$, where $\kappa = \frac{\lambda_o}{\xi_{co}}$ designates the Ginzburg–Landau parameter.

4 Results and discussion

4.1 Structure and microstructure analyses

The collected XRD patterns of Bi-0.0, Bi-0.1, and Bi-0.2 ceramics are shown in Fig. 1. The reflection peaks denoted by "3" correspond to Bi-2223 phase and those denoted by "2" are allied with Bi-2212 phase. For the three ceramics, most peaks correspond to the Bi-2223 phase and a small number of peaks agree with the Bi-2212 phase. A minor peak intensity of the non-superconducting Ca_2PbO_4 phase is also observed in the free and ZrO_2 -added ceramics. Within the sensitivity limit of the XRD instrument and the too-low concentration of additives, no ZrO_2 peaks were detected in the patterns. The XRD patterns also attest that ZrO_2 addition does not provoke any shift in the diffraction angles positions, which indicate that ZrO_2 did not enter the crystal structure. Intensities (I) of peaks are commonly utilized to quantify the volume fraction of Bi-2223, Bi-2212, and Ca_2PbO_4 phases as follows [14, 15]:

$$V_{Bi-2223} = \frac{\sum I_{Bi-2223}}{\sum I_{Bi-2212} + \sum I_{Bi-2223} + I_{Ca_2PbO_4}} \times 100,$$

$$V_{Bi-2212} = \frac{\sum I_{Bi-2212}}{\sum I_{Bi-2212} + \sum I_{Bi-2223} + I_{Ca_2PbO_4}} \times 100,$$

$$V_{Ca_2PbO_4} = \frac{I_{Ca_2PbO_4}}{\sum I_{Bi-2212} + \sum I_{Bi-2223} + I_{Ca_2PbO_4}} \times 100.$$

In these relations $\sum I_{Bi-2223}$ and $\sum I_{Bi-2212}$ denote the sum of intensities of Bi-2223 and Bi-2212 phases, respectively. The volume fractions of the three existent phases are determined. Both free-added and ZrO_2 -added ceramics exhibit almost identical volume fractions of the Bi-2223, Bi-2212, and Ca_2PbO_4 phases of about 86%, 13%, and 1%, respectively. A slight quantity of ZrO_2 added to Bi-based superconductor ceramics does not impress the traits of the liquid produced at the reaction temperature and does not alter the growth kinetics of Bi-2223.

SEM micrographs exposed in Fig. 2 illustrate the morphology of Bi-0.0, Bi-0.1, and Bi-0.2 ceramics. The three micrographs show a compacted granular structure formed practically by micrometric grains with plate-like form signs of the Bi-2223 phase [14, 15]. No perceived change in the grain size is detected as a result of low additions of ZrO_2 . Micrographs of Bi-0.0 and Bi-0.1 ceramics show a softly best textural structure compared to the Bi-0.2 one. The microstructural trait of ZrO_2 nanoparticles was inspected by TEM and the findings illustrate particles having an average size of about 10 to 20 nm (Inset (a) of Fig. 3). Figure 3 illustrates low magnification TEM image photographed on Bi-2223 phase for ceramic B-0.1. Nanometric inhomogeneities with an average size of about 15 nm incorporated in the Bi-2223 phase are clearly manifested. The EDX spectrum (Inset (b) of Fig. 3) verified the occurrence of Y, Ba, Cu, and O elements besides the Zr element. These results attest that the observed inhomogeneities encompass Zirconium. The fine grain structure bound in the superconducting grains could lead to a rise in the density of grain boundaries (GB) and fine-scale disorders in the superconducting grains. These microstructural modifications alter the intragranular properties, and as a consequence, could affect the FIC behavior and or raise the sites of vortices trapping.

4.2 Excess conductivity analysis

Before moving towards the excess conductivity analysis, we first present the variations of electrical resistivity with temperature ($\rho(T)$) for the three ceramics. Figure 4 shows typical metallic behavior ($d\rho/dT > 0$) of resistivity, with room temperature resistivity (ρ_{285K}) of about 1.78, 1.34, and 1.40

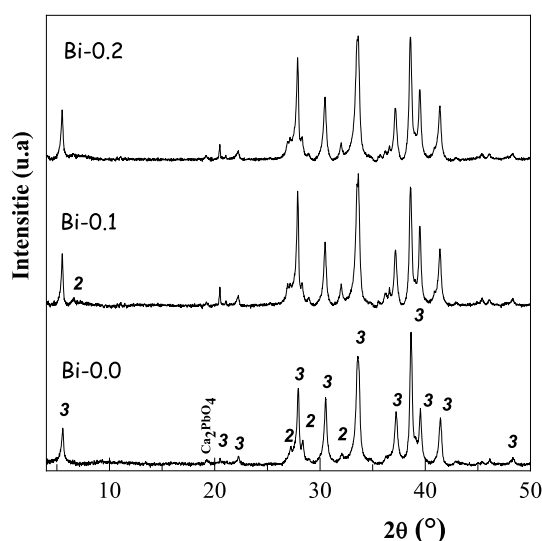


Fig. 1 XRD patterns of Bi-0.0, Bi-0.1, and Bi-0.2 ceramics

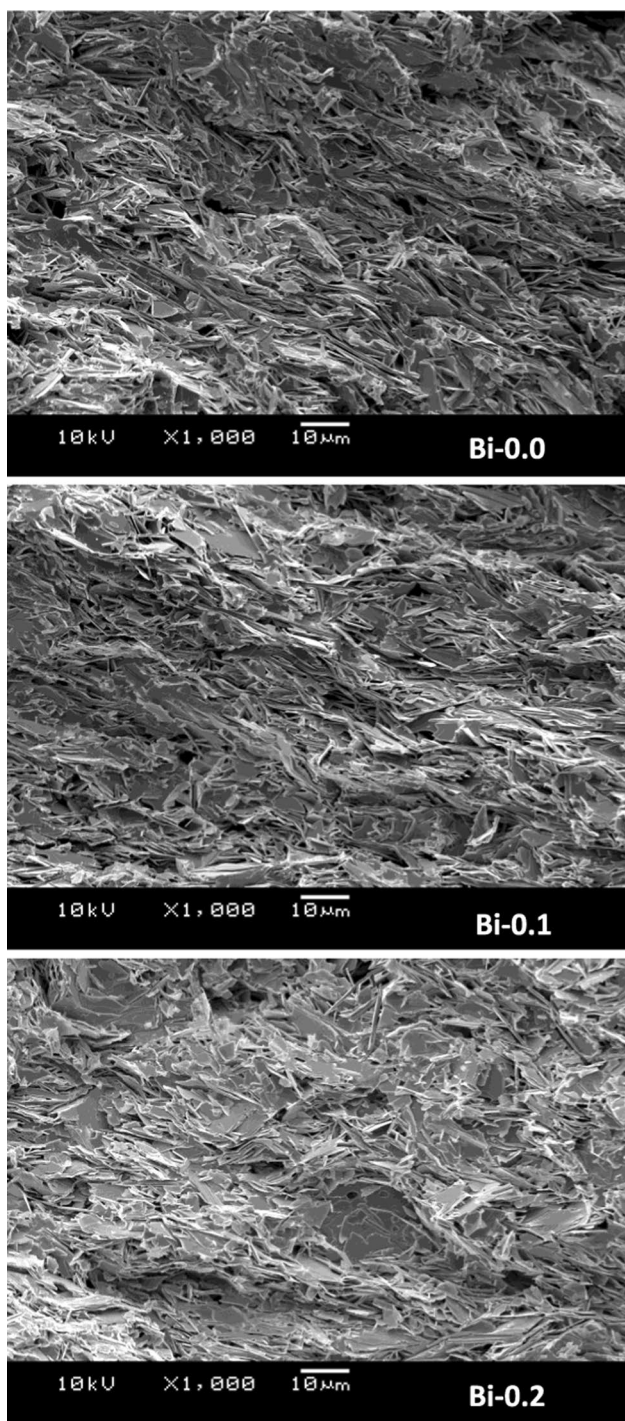


Fig. 2 SEM images of Bi-0.0, Bi-0.1, and Bi-0.2 ceramics

Ω-cm for Bi-0.0, Bi-0.1, and Bi-0.2 ceramics, respectively. From room temperature and going down till temperature T^s that is related to a pseudogap opening [22], the resistivity deviates from the linear behavior. Some models have been proposed to describe the mechanism of conduction in the normal state of HTS, viz., the variable range hopping

(VRH), the variable range hopping with Coulomb interactions (CG) [38, 39], and the bipolaron [40]. To explore the metal-like behavior of $\rho(T)$ in the normal state, the CG and bipolaron models were tested and the results of fitting reveal that conduction characteristics are more consistent with the bipolaron regime. In copper oxide superconductors, bipolaron could be generated via an interaction between optical phonons (with energy $\hbar\omega$) and holes at temperatures below T_c [41]. This model supposes that the fraction of carriers is localized by disorder and expects a $\rho(T)$ variation as:

$$\rho(T) = \rho_o \frac{\exp(-\omega/T) + (T/T_L)^2}{\left[1 + M\left(\frac{T}{T_c}\right)(1 - \exp(-T_o/T))^{1/2} \exp\left(-\left(\frac{T^*}{T}\right)\right)\right]}$$

ρ_o and T_o depends on the number of carriers localized by the disorders and the doping concentration and $M \approx 6$ is the ratio of bipolaron and polaron masses. The temperature T_o is very close to T_c and could be extracted from $\frac{d\rho(T)}{dT}$ plot. $T_L = (b/a)^{1/2}$ is temperature independent parameter, varies with optical phonon scattering (b) and itinerant carrier scattering (a) contributions, and the temperature T^* is a characteristic of the material. The fitting of the bipolaron model for our samples is represented in Fig. 4 at right. The Bipolaron model matches perfectly our experimental data. Table 2 lists the parameters resulting from fitting. It is noticed that the temperature T^s that points the divergence of normal state resistivity $\rho(T)$ from the linear dependence is consistent with the T^* temperature obtained by fitting using the Bipolaron model. Both ZrO_2 inhomogeneities embedded inside the superconducting grains and the generated defects yield an increase in disorders. Hence, the number of localized carriers rises and superconductivity suppresses.

From room temperature to T^s the measured resistivity could be described by a linear decay $\rho_n(T) = \rho_{rem} + \rho_{TC}T$. ρ_{rem} terms the remanent resistivity and is attributed to the scattering phenomena. Whereas ρ_{TC} denotes the resistivity temperature coefficient and reflects the intrinsic electronic interaction. The extracted values of ρ_{rem} and ρ_{TC} for both products are registered in Table 3. The lower values of ρ_{rem} and ρ_{TC} registered in the Bi-0.1 ceramic imply the constructive effect of ZrO_2 on the electrical conductivity. By lowering the temperature below T_{cmf} , the coupling energy among grains overcomes the thermal energy, and hence, a superconducting order over the whole granular structure will be settled at T_{co} (zero resistivity temperature). We note here that T_{cmf} is regarded as being the temperature of the main peak spotted in the derivative, $\frac{d\rho}{dT}$ vs T plot. The estimated values of T_{cmf} are listed in Table 3. T_{cmf} is slightly weakened when ZrO_2 content increases up to 0.2 wt.%. The disorder generated by ZrO_2 addition could be one the possible causes of the reduction of T_{cmf} in HTS compounds [42, 43].

Fig. 3 TEM image of Bi-0.1 ceramic showing nano-inhomogeneities. Insets **(a)** micrograph showing the nanosized ZrO₂ particles used in this study and **b** EDXS spectrum taken from an area of Fig. 3 revealed Zr element

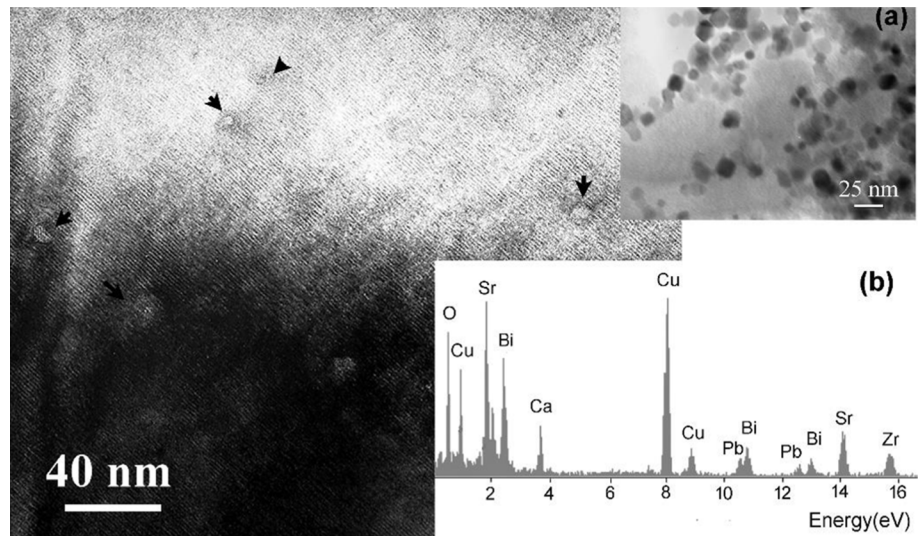


Fig. 4 (Left) Resistivity dependence on the temperature and (Right) fitting the resistivity data with bipolaron model for Bi-0.0, Bi-0.1, and Bi-0.2 ceramics

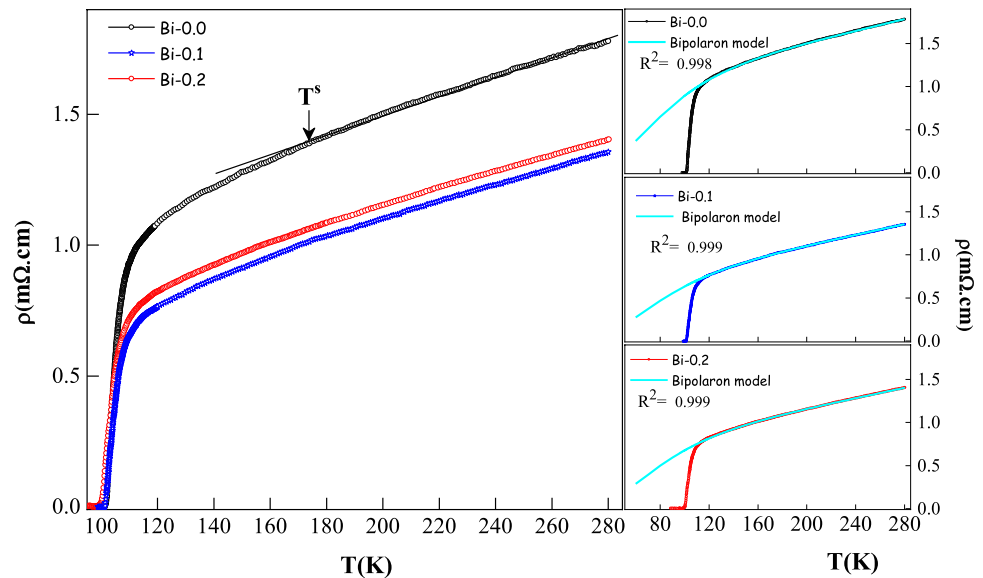


Table 2 Results of the Bipolaron fitting for Bi-0.0, Bi-0.1, and Bi-0.2 samples

Sample	ρ_0 (mΩ.cm)	ω (K)	T_L (K)	T^* (K)
Bi-0.0	9.9	226.7	364.7	179.4
Bi-0.1	6.8	248.1	312.9	169.7
Bi-0.2	7.3	264.7	331.4	167.3

The analysis of excess conductivity $\Delta\sigma = A_F t^{\lambda_D}$ is done by considering logarithm form on both sides: $\ln\Delta\sigma = \ln A_F + \lambda_D \ln t$. The straight-line relationship presents an easy method to determine λ_D and A_F . Indeed, the slope of the curve is λ_D and the intercept of the straight-line extrapolation with the \ln axis helps us to extract the value of the amplitude A_F . Figure 5 shows the plots

Table 3 Parameters extracted from the resistivity measurements and excess conductivity analysis for Bi-0.0, Bi-0.1 and Bi-0.2

Analysis	Parameters	Ceramic		
		Bi-0.0	Bi-0.1	Bi-0.2
Resistivity	ρ_{285} (Ω cm)	1.78	1.34	1.40
	ρ_{rem} (Ω cm)	0.69	0.47	0.47
	ρ_{TC} (Ω cm/K)	0.0040	0.0031	0.0034
	T_{co} (K)	101.4	101.5	99.7
	T_c^{mf} (K)	104.5	104.6	104
Excess conductivity	T_G (K)	105.3	105.3	105
	T_{LD} (K)	106.8	107.5	106.9
	$T_{2D \times 1D}$ (K)	125.1	130.7	128.6
	$T_{1D \times SW}$ (K)	147.1	150.6	142.1
	N_G (K)	0.0077	0.0067	0.0078

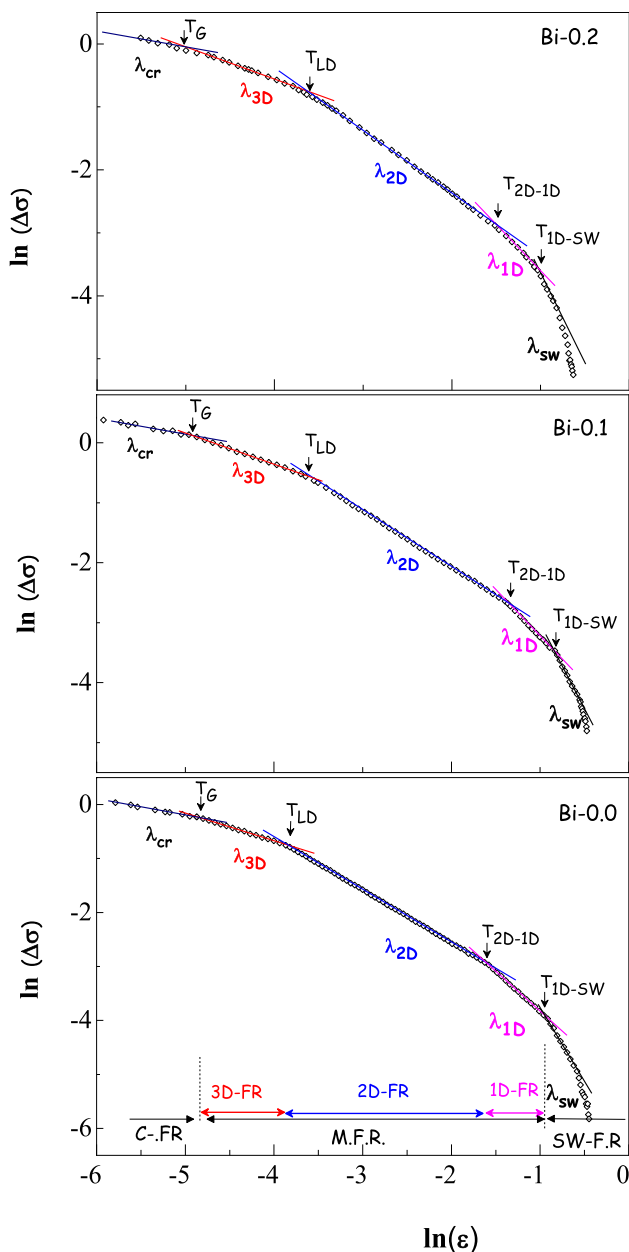
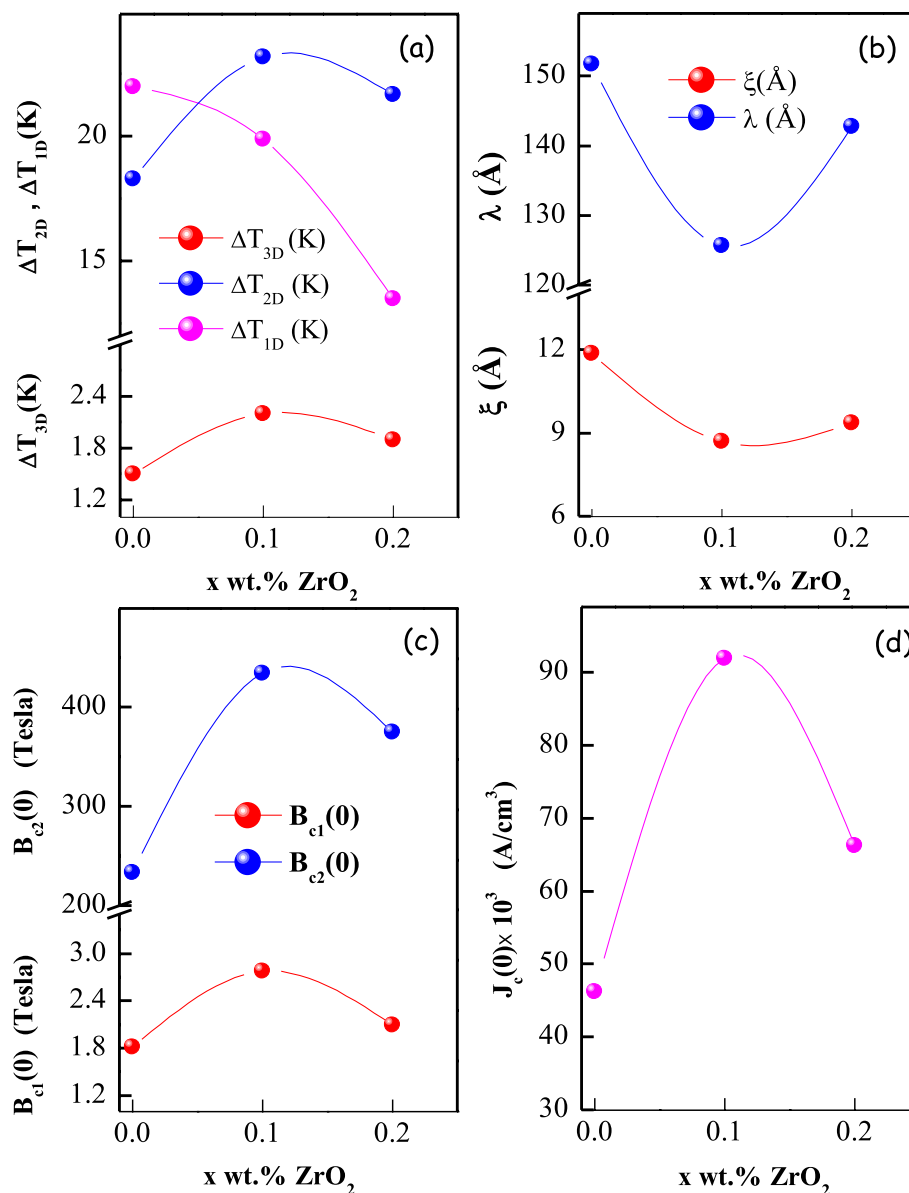


Fig. 5 Plots of $\ln(\Delta\sigma)$ versus $\ln(\epsilon)$ for Bi-0.0, Bi-0.1, and Bi-0.2 ceramics. The fitting of the experimental \ln - \ln curves is represented by solid color straight lines. λ_{cr} , λ_{3D} , λ_{2D} , λ_{1D} and λ_{sw} refer to critical, three, two one, and short-wave dimensions of conduction

of $\ln\Delta\sigma$ vs $\ln t$ of Bi-0.0, Bi-0.1, and Bi-0.2 ceramics. The adjustment of the experimental \ln - \ln data with the theoretical predictions is represented by solid straight lines with different colors for MFR. Each plot could be fragmented into five straight lines corresponding to the slopes $\lambda_{2cr} = -1/3$ for critical fluctuation region, $\lambda_{sw} \sim -3$ for short-wave fluctuation regime and $\lambda_D = -0.5, -1,$ and -1.5 for fluctuation of conductivity in 3D, 2D, and 1D. These behaviors of fragmentation are often observed in

the FIC of various HTS. In references [22, 25–27], FIC was analyzed by four fluctuation regions, viz., critical, short-wave, 3D, and 2D fluctuation regimes. In references [23, 28], the authors reveal that the 1D fluctuation regime participates also along with the four cited regimes. Transition and crossover temperatures as T_{co} , T_{cmf} , T_G , T_{LD} , $T_{2D \times 1D}$, and $T_{1D \times SW}$ for the three ceramics are listed in Table 3. Attainment of higher temperatures in the Bi-0.1 ceramic notifies a better superconducting performance as compared to others. When the temperature is below T_G and comes closer to T_{cmf} , the fluctuation in the amplitude of order parameter ψ grows up to become approximately of the same order as itself. Therefore, a large fluctuation governs the system, and the 3D-XY model previously established for the superfluid transition in liquid ^4He , describes well this critical fluctuation regime [44, 45]. Whereas, far from T_{cmf} and near T_c^{on} at the knee of $\rho(T)$ curve (superconducting onset temperature), the fluctuation of the order parameter is analogous to the coherence length. In this region, the thermal energy is as high to hold steady the formed cooper pairs as long as possible, and as a consequence, SW fluctuations will take place. In the mean-field region, all curves advertise 3D, 2D, and 1D conductivity fluctuations. The last regime is ascribed to the survival of conducting charge strips [46]. The width of this regime of fluctuation is shortened with ZrO_2 addition. Microscopic and mesoscopic inhomogeneities could destabilize the conducting charge strips and hence shrink the 1D regime width [23]. We notice that the 2D fluctuation regime is wider compared to the 3D one. This is clear evidence that the superconductivity mainly occurs in the CuO_2 planes. BSCCO is an anisotropic system, its layered structure is formed by alternating low-conductivity layers enfolded by high-conductive CuO_2 planes, in which the charge carriers have the tendency to flow easily before the superconducting order extending over a long range. By further reducing the temperature, the charge carriers can jump between the CuO_2 planes in 3D, and thus a motion in the entire system will be established before a global superconducting state settles beyond T_{co} . Noting that following the ZrO_2 addition, the 2D regime width increases, and that of the 3D regime somewhat spreads over a broader region (Fig. 6a). This behavior may be attributed to the superconducting grains coupling. The higher the GB density is, the broader the 2D regime of fluctuation and the smaller thickness of effective layers of the 2D system, and therefore more 3D regime appears earlier. Indeed, our ceramics are formed by superconducting crystallites randomly oriented, and thus the microscopic parameters as d and ξ_{co} are regarded as effectual parameters of polycrystalline medium [23, 47]. Based on the crossover temperature T_G and the amplitude expressions for 2D and 3D fluctuation regimes

Fig. 6 Variations of (a) 2D and 3D conductivity fluctuation regions, b microscopic physical characteristics ξ_{co} and λ_o and c critical physical parameters $B_{c1}(0)$, $B_{c2}(0)$ and d $J_c(0)$ at 0 K as a function of the ZrO_2 nano content



and given that the factor γ frequently taken about 10, d and ξ_{co} and the thermodynamic critical magnetic field B_{co} and $\lambda(\text{\AA})$ are extracted for zero absolute temperature. The lower value of d particularly for the Bi-0.1 ceramic proves an enhancement of the core density and a better link between grains (Fig. 6b). Our estimated values of ξ_{co} are comparable to those stated by other groups [23, 48]. Due to the polycrystalline nature of these ceramics, d and ξ_{co} values were higher than those reported in thin film and monocrystal [49]. Besides, the λ values were less than those reported in Ref [23], hence reflecting the best shielding of flux lines particularly in Bi-0.1 ceramic. Once the penetration depth is estimated with the help of the B_{co} expression, values of $B_{c1}(0)$, $B_{c2}(0)$, and $J_c(0)$

were estimated and depicted in Fig. 6c and Fig. 6d. As observed these three critical parameters are enhanced with the addition of ZrO_2 , and the Bi-0.1 ceramic reveals the best values. The strengthening of these critical parameters is chiefly attributed to the damping in the motion of vortices through improving the flux trapping sites inside the ceramic artificially introduced by the addition of ZrO_2 nanoparticles. The Twin boundaries, the grain boundaries and the superconducting/nanophase interface, and the local strained regions are stated as strong flux pinning sites (SFPC) [50, 51]. Noticeably the $J_c(0)$ values for our samples are of an order of magnitude higher than those reported in La-Substituted Ca in (Bi, Pb):2223 [52].

4.3 Critical current density and flux pinning mechanism

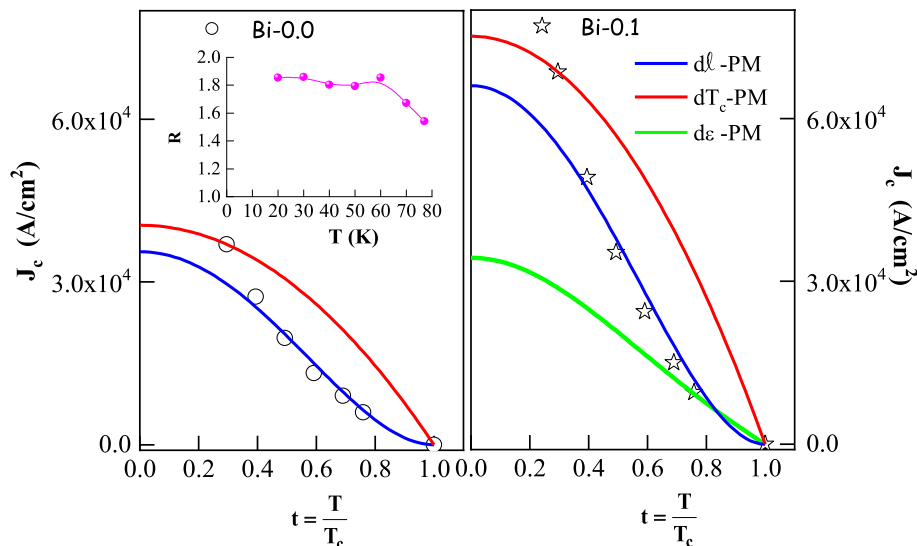
In the rest of the paper, we assess the critical current density versus temperature $J_c(T)$. This later is determined with the help of isothermal magnetization measurements and using the beam model [53]. Based on the above-cited results we consider $J_c(T)$ of free and 0.1 wt.% added ceramics. The values of J_c of Bi-0.1 was compared to those of Bi-0.0 for different temperatures and the plot of the ratio $R = \frac{J_{c, Bi-0.1}(T)}{J_{c, Bi-0.0}(T)}$ is shown in the inset of Fig. 7. The Bi-0.1 ceramic was found to exhibit the highest values of J_c over the whole range of measurement temperature, suggesting the best flux pinning property in this ceramic. Almost analogous values of R evaluated at 10 K are reported in the literature for polycrystalline (Bi,Pb)2223 superconductors doped with TiO_2 -nanorod [54] and NP SiC [55]. However, the obtained values of self-field J_c measured at 77 K are larger compared to the best data stated in (Bi,Pb)2223 tape/ $CoFe_2O_4$ [20], (Bi, Pb)2223 tape/ NiF_2 [56], (Bi,Pb)2223 tape/ Co_3O_4 [13] and (Bi, Pb):2223 tape/ Bi_2O_3 [57]. Cores that govern the pinning of flux lines are (1) spatial variations of the mean free path of charge carrier owing to the scattering by normal phase noted δl , (2) spatial variations of the κ parameter connected with a random distribution of the critical temperature noted δT_c and (3) stress/strain field noted $\delta \epsilon$. Analysis of the $J_c(T)$ was performed using the collective flux pinning model [58], where $J_c(T)$ is expressed against the reduced temperature ($t = T/T_{co}$) as: $J_c = J_{co}(1 - t)^\alpha(1 + t)^\beta$, and for δT_c , δl , and $\delta \epsilon$ trapping sites $J_c = J_{co}(1 - t)^{7/6}(1 + t)^{5/6}$ [59, 60], $J_c = J_{co}(1 - t)^{5/2}(1 + t)^{-1/2}$, and $J_c = J_{co}(1 - t)^{7/6}(1 + t)^{-11/6}$ [61], respectively. Analysis of J_c versus t by means of δT_c , δl , and $\delta \epsilon$ mechanisms was done for the self-magnetic field (Fig. 7). As seen the $J_c(t)$ trends can be ascribed by the

contribution of δT_c core for both ceramics at low temperature and at high temperature, mainly δl core validate $J_c(t)$ behavior over a larger range of the considered temperature. The above results sign that the ZrO_2 addition betters the flux pinning mainly by normal phase at elevated temperature. Normal phases dispersed inside the superconducting matrix are frequently proven to be dominant in the FP mechanism. When the normal phase is larger than the coherence length, the pinning mostly arises from the interfaces among the superconducting grain and the normal phases and/or from the generated defects. Normal phases may be generated naturally as Ca_2PbO_4 phase or artificially by adding a suitable concentration of fine nanoparticles such as Zr-rich inhomogeneities in our case. Hence, the former phase seems to be responsible for spatial variation of the mean free path of charge carriers (δl core) for Bi-0.0 ceramic, and for Bi-0.1 ceramic both Ca_2PbO_4 and Zr-rich inhomogeneities compete in δl pinning core to produce a positive competitive effect in reinforcing pinning properties.

5 Conclusion

Using the solid-state reaction process, we fabricated Bi-2223 ceramics with the addition of zirconia (ZrO_2) nanoparticles of about 20 nm in size. The proportion x of ZrO_2 per the total mass of superconductor ranged from 0 wt.% to 0.2 wt.%. We report the intragrain critical current density (J_c), pinning mechanisms, and thermal fluctuations induced excess conductivity. The main Bi-2223 phase along with Bi-2212 and insignificant Ca_2PbO_4 phases are identified in all ceramics. The Bi-2223 and Bi-2212 phase volume fractions are not impacted by the ZrO_2 addition, and they are about 86% and 13%, respectively. Plots of resistivity against temperature

Fig. 7 Reduced temperature dependence of the J_c for Bi-0.0 and Bi-0.1 ceramics. The red, blue, and green lines are theoretical curves according to δT_c , δl , and $\delta \epsilon$ pinning cores. Inset shows the ratio R between $J_c(T)$ of Bi-0.1 ceramic and Bi-0.0



evidenced that the critical temperature for the transition to the superconductor state, T_{co} , slightly decreases from 101.4 to 99.7 K when the NP-ZrO₂ content is increasing from 0 wt.% to 0.2 wt.%. With the help of the Aslamazov–Larkin model, we assessed, thorough excess conductivity curves, the crossover temperatures between different regimes of conductivity, the coherence length, the penetration depth as well as $B_{c1}(0)$ and $B_{c2}(0)$ values for all the ceramics. It was established that NP-ZrO₂ upgrades $B_{c1}(0)$ and $B_{c2}(0)$ and the elevated values are obtained for ceramic added with an amount of 0.1 wt.% NP-ZrO₂. We also found that the $J_c(T)$ is raised by NP-ZrO₂ addition and thereby the strengthening of δl pinning cores resulted in the improvement of the flux pinning ability.

Acknowledgements The authors acknowledged the Institute for Research and Medical Consultations (IRMC) and Basic and Applied Scientific Research Center (BASRC) of Imam Abdulrahman Bin Faisal University (Dammam, Saudi Arabia) for providing laboratory facilities.

Author contributions MZ: formal analysis. MBS: supervision. YS: validation, formal analysis, writing—review and editing. HSA: formal analysis. FBA: conceptualization, methodology, investigation, writing—original draft, writing—review and editing, supervision.

Funding No funding was received for this study.

Data availability All data generated or analyzed during this study are included in this published article.

Declarations

Conflict of interest The authors have no competing interests to declare that are relevant to the content of this article.

References

1. M. Yazdani-Asrami, M. Z., W. Yuan, Challenges for developing high temperature superconducting ring magnets for rotating electric machine applications in future electric aircrafts, *J. Magn. Magn.* **522**, 167543 (2021)
2. L.L. Kaczmarek, R.I. Jsselsteijn, V. Zakosarenko, A. Chwala, H.G. Meyer, M. Meyer, R. Stolz, Advanced HTS DC SQUIDS with step-edge Josephson junctions for geophysical applications. *IEEE Trans. Appl. Supercond.* **28**, 1601805 (2018)
3. A. Biju, P. Guruswamy, U. Syamaprasad, Influence of Pb on structural and superconducting properties of rare earth modified Bi₂Sr₂CaCu₂O_y, *Physica C* **466**, 23 (2007)
4. F. Ben Azzouz, A. M'chirgui, N. Naït Slimen, M. Ben Salem, Effect of substantial addition of PbO on liquid phase conversion during the final processing of (Bi,Pb)-2223 superconductors, *Physica C*, **416**, 115 (2004)
5. N. A. A. Yahya, R. Abd-Shukor, Effect of nano-sized PbO on the transport critical current density of (Bi_{1.6}Pb_{0.4}Sr₂Ca₂Cu₃O₁₀)/Ag tapes, *Ceram. Int.* **40**, 5197 (2014)
6. H.F. Arani, S. Baghshahi, A. Sedghi, D. Stornaiuolo, F. Tafuri, D. Massarotti, N.R. Noori, The influence of heat treatment on the microstructure, flux pinning and magnetic properties of bulk BSCCO samples prepared by sol-gel route. *Ceram. Int.* **44**, 5209 (2018)
7. A. Sedky, A.M. Ali, H.H. Somaily, Effect melting time on the excess conductivity and critical parameters of BSCCO cooper oxide system. *J. Supercond. Nov. Magn.* **33**, 2963 (2020)
8. L. Pérez-Acosta, E. Govea-Alcaide, J.G. Noudem, I.F. Machado, S.H. Masunaga, R.F. Jardim, Highly dense and textured superconducting (Bi, Pb)₂Sr₂Ca₂Cu₃O_{10.8} ceramics amples processed by spark-plasma texturing. *Ceram. Int.* **42**, 13248 (2016)
9. M.S. Shalaby, M.H. Hamed, N.M. Yousif, H.M. Hashem, The impact of the addition of Bi₂Te₃ nanoparticles on the structural and the magnetic properties of the Bi-2223 high-Tc superconductor. *Ceram. Int.* **47**, 25236 (2021)
10. H. Baqiah, S. A. Halim, M. I. Adam, S. K. Chen, S. S. H. Ravandi, M. A. M. Faisal, M. M. Kamarulzaman, M. Hanif, The effect of magnetic nanoparticle addition on the superconducting properties of Bi_{1.6}Pb_{0.4}Sr₂Ca₂Cu₂O₈ superconductors, *J. Solid State Sci. Technol.* **17**, 81 (2009)
11. H.F. Arania, S. Baghshahi, A. Sedghi, N.R. Noori, Enhancement in the performance of BSCCO (Bi-2223) superconductor with functionalized TiO₂ nanorod additive. *Ceram. Int.* **45**, 21878 (2019)
12. A. Sedky, A. Salah, Fluctuation, diamagnetic transition, and FTIR spectra of La substituting Ca in (Bi, Pb): 2223 superconductor. *J. Supercond. Nov. Magn.* **33**, 3705 (2020)
13. A. N. Jannah, H. Abdullah, R. Abd-Shukor, Enhanced transport critical current density in Ag-sheathed (Bi_{1.6}Pb_{0.4})Sr₂Ca₂Cu₃O_y superconductor tapes with different nano-sized Co₃O₄ addition, *J. Supercond. Nov. Magn.* **28**, 1471 (2015)
14. Ö. Bilgili, M. Yurddaskal, Effects of graphene oxide doping on magnetic and structural properties of Bi_{1.6}Pb_{0.4}Sr₂Ca₂Cu₃O_y superconductor, *J. Electron. Mater.* **50**, 4999 (2021)
15. A. Ghattas, M. Annabi, M. Zouaoui, F. Ben Azzouz, M. Ben Salem, Flux pinning by Al-based nano particles embedded in polycrystalline (Bi, Pb)-2223 superconductors, *Physica C*, **468**, 31 (2008)
16. W. Abdeen, S. Marahba, R. Awad, A. I. Abou Aly, I. H. Ibrahim, M. Matar, Electrical and mechanical properties of (Bi,Pb)-2223 substituted by holmium, *J. Adv. Ceram.* **5**, 54 (2016)
17. N.A. Yahya, A. Al-Sharabi, N.R. MohdSui, W.S. Chiu, R. Abd-Shukor, Enhanced transport critical current density of (Bi, Pb)-2223/Ag superconductor tapes added with nano-sized Bi₂O₃. *Ceram. Int.* **42**, 18347 (2016)
18. G. Kirat, O. Kızılaslan, M.A. Aksan, Effect of the Er-substitution on critical current density in glass-ceramic Bi₂Sr₂Ca₂(Cu_{3-x}Er_x)O_{10.8} superconducting system. *Ceram. Int.* **42**, 15072 (2016)
19. S. Safran, H. Ozturk, F. Bulut, O. Ozturk, The influence of repelletization and heat treatment on physical, superconducting, magnetic and micro-mechanical properties of bulk BSCCO samples prepared by ammonium nitrate precipitation method. *Ceram. Int.* **43**, 15586 (2017)
20. M. Hafiz, R. Abd-Shukor, Transport critical current density of (Bi_{1.6}Pb_{0.4})Sr₂Ca₂Cu₃O₁₀/Ag superconductor tapes with addition of nanosized CoFe₂O₄, *Appl. Phys. A* **120**, 1573 (2015)
21. H. Oztürk, S. Safran, Effects of carbon-encapsulated nano boron addition on superconducting parameters of BSCCO. *J. Alloys Compd.* **731**, 831 (2018)
22. A. Aftabi, M. Mozaffari, Fluctuation induced conductivity and pseudogap state studies of Bi_{1.6}Pb_{0.4}Sr₂Ca₂Cu₃O_{10+δ} superconductor added with ZnO nanoparticles, *Sci. Rep.* **11**, 4341 (2021)
23. N. Loudhaief, M. Ben Salem, H. Labiadh, M. Zouaoui, Electrical properties and fluctuation induced conductivity studies of Bi-based superconductors added by CuS nanoparticles

- synthesized through the aqueous route. *Mater. Chem. Phys.* **242**, 122464 (2020)
24. A. Harabor, P. Rotaru, N. A. Harabor, Effect of Ni substitute in off-stoichiometric Bi(Pb)-Sr-Ca-Cu(Ni)-O superconductor. Excess conductivity, XRD analysis and thermal behaviour, *Ceram. Int.* **45**, 2742 (2019)
 25. R. Awad, H.T. Rahal, A.M. Abdel-Gaber, A.I. Abou-Aly, Excess conductivity and magnetoconductivity analysis of $(\text{NiO})_x(\text{Bi, Pb})$ -2223 superconducting phase. *J. Supercond. Nov. Magn.* **32**, 2733 (2019)
 26. K. Habanjar, F. El Haj Hassan, R. Awad, Comparative studies for the physical properties of superconducting $(\text{BaSnO}_3)_x(\text{Bi, Pb})$ -2223 samples determined from excess conductivity and thermoelectric power analysis, *Mater. Res. Express* **6**, 096001 (2019)
 27. M. Roumié, W. Abdeen, R. Awad, M. Korek, I. Hassan, R. Mawassi, Excess conductivity Analysis of $\text{Bi}_{1.8}\text{Pb}_{0.4}\text{Sr}_2\text{Ca}_2\text{Cu}_3\text{O}_{10+\delta}$ Added with Nano-ZnO and Nano- Fe_2O_3 , *J. Low Temp. Phys.* **174**, 45 (2014)
 28. N. Loudhaief, M. Ben Salem, M. Zouaoui, Synthesis and characterization of Eu- and La-doped CuS nanoparticles and their effects on the electrical properties of $(\text{Bi, Pb})_2\text{Sr}_2\text{Ca}_2\text{Cu}_3\text{O}_d$ superconductor, *J. Mater. Sci.: Mater. Electron.* **32**, 453 (2021)
 29. R. Sigwadi, M. Dhlamini, T. Mokrani, F. Nemaivhola, Preparation of a high surface area zirconium oxide for fuel cell application. *Int. J. Mech. Mater. Eng.* **14**(1), 1 (2019)
 30. Z. Liang, S. Zhou, W. Cai, X. Fu, H. Ning, J. Chen, W. Yuan, Z. Zhu, R. Yao, J. Peng, Zirconium-aluminum-oxide dielectric layer with high dielectric and relatively low leakage prepared by spin-coating and the application in thin-film transistor. *Coatings* **10**(3), 282 (2020)
 31. E. De la Rosa-Cruz, L.A. Diaz-Torres, P. Salas, V.M. Castano, J.M. Hernandez, Evidence of non-radiative energy transfer from the host to the active ions in monoclinic $\text{ZrO}_2: \text{Sm}^{+3}$. *J. Phys. D Appl. Phys.* **34**, 83 (2001)
 32. N. Tabassum, D. Kumar, D. Verma, R.A. Bohara, M.P. Singh, Zirconium oxide (ZrO_2) nanoparticles from antibacterial activity to cytotoxicity: a next-generation of multifunctional nanoparticles. *Mater. Today Commun.* **26**, 102156 (2021)
 33. C. Li, S. Zhang, L. Gao, Q. Hao, L. Bai, P. Zhang, Doping effects of ZrO_2 nanoparticles on the superconducting properties of Bi-2212 tapes. *J Mater Sci: Mater Electron* **26**, 3583 (2015)
 34. M. Zouaoui, A. Ghattas, M. Annabi, F.B. Azzouz, M.B. Salem, Effect of nano-size ZrO_2 addition on the flux pinning properties of (Bi, Pb)-2223 superconductor. *Supercond. Sci. Technol.* **21**, 125005 (2008)
 35. M. Zouaoui, L. Bessais, M. Ben Salem, Thermally activated dissipation and pinning mechanisms in a Bi-2223 superconductor with the addition of nanosized ZrO_2 particles. *Supercond. Sci. Technol.* **23**, 095013 (2010)
 36. L.G. Aslamazov, I.A. Larkin, The influence of fluctuation pairing of electrons on the conductivity of normal metal. *Phys. Lett.* **26**, 238 (1968)
 37. W.E. Lawrence, S. Doniach, In: E. Kanda (Ed.), *Proceedings of the Twelfth International Conference on Low Temperature Physics (Kyoto, 1970)*, Keigaku, Tokyo, 1971, p. 361
 38. N.F. Mott, *Conduction in non-crystalline materials* (Clarendon press, Oxford, 1993)
 39. A.L. Efros, B.I. Shklovskii, Coulomb gap and low temperature conductivity of disordered systems. *J. Phys. C* **8**, L49 (1975)
 40. A.S. Alexandrov, A.M. Bratkovsky, N.F. Mott, Hall effect and resistivity of high- T_c oxides in the bipolaron model. *Phy. Rev. Lett.* **72**, 1734 (1994)
 41. A.S. Alexandrov, V.N. Zavaritsky, S. Dzhumanov, Hall effect and resistivity in underdoped cuprates. *Phys. Rev. B* **69**, 052505 (2004)
 42. A.M. Ali, A. Sedky, H. Algarni, M.A. Sayed, Argon annealing and oxygen purity affect structural and critical parameters of YBCO copper oxide system. *J. Low Temp. Phys.* **197**, 445 (2019)
 43. M. Tariq, M. Zubair, The Effect of Preparation Temperature on the Superconducting Parameters of $\text{Cu}_{1-x}\text{Tl}_x\text{Ba}_2\text{Ca}_2\text{Cu}_3\text{O}_{10-\delta}$ Superconductor, *J Supercond. Nov. Magn.* **28**, 1455 (2015)
 44. J. Roa-Rojas, R.M. Costa, P. Pureur, Pairing transition, coherence transition, and the irreversibility line in granular $\text{GdBa}_2\text{Cu}_3\text{O}_{7-\delta}$. *Phys. Rev. B* **61**, 12457 (2000)
 45. A.R. Jurelo, R.M. Costa, P.R. Júnior, F.C. Serbena, Fluctuation conductivity and phase separation in polycrystalline $\text{Y}_{1-x}\text{Ce}_x\text{Ba}_2\text{Cu}_3\text{O}_{7-\delta}$ superconductors. *J. Supercond. Nov. Magn.* **23**, 247 (2010)
 46. A. Bianconi, A. Valletta, A. Perali, N.L. Saini, Superconductivity of a striped phase at the atomic limit. *Physica C* **296**, 269 (1998)
 47. A.A. Khurram, M. Mumtaz, N.A. Khan, M.M. Ahadian, A. Irajizad, The effect of grain size on the fluctuation-induced conductivity of $\text{Cu}_{1-x}\text{Tl}_x\text{Ba}_2\text{Ca}_3\text{Cu}_4\text{O}_{12-\delta}$ superconductor thin films. *Supercond. Sci. Technol.* **20**, 742 (2007)
 48. R. Awad, H.T. Rahal, A.M. Abdel-Gaber, A.I. Abou-Aly, Excess Conductivity and Magnetoconductivity Analysis of $(\text{NiO})_x(\text{Bi, Pb})$ -2223 Superconducting Phase. *J. Supercond. Nov. Magn.* **32**, 2733 (2019)
 49. L. Fruchter, I. Sfar, F. Bouquet, Z.Z. Li, H. Raffy, Nonlinear excess conductivity of $\text{Bi}_2\text{Sr}_2\text{Ca}_{n-1}\text{Cu}_n\text{O}_{2n+4+x}$ ($n=1,2$) thin films. *Phys. Rev. B.* **69**, 144511 (2004)
 50. J. Plain, T. Puig, F. Sandiumenge, X. Obradors, J. Rabier, Microstructural influence on critical currents and irreversibility line in melt-textured $\text{YBa}_2\text{Cu}_3\text{O}_{7-x}$ reannealed at high oxygen pressure. *Phys. Rev. B: Condens. Matter* **65**, 104526 (2002)
 51. M.K. Ben Salem, E. Hannachi, Y. Slimani, A. Hamrita, M. Zouaoui, L. Bessais, M. Ben Salem, F. Ben Azzouz, SiO_2 nanoparticles addition effect on microstructure and pinning properties in $\text{YBa}_2\text{Cu}_3\text{O}_y$, *Ceram. Int.* **40**, 4953 (2014)
 52. A. Sedky, A. Salah, Comparative study of the effects of La-substituted Ca in (Bi, Pb):2212 and (Bi, Pb):2223 superconductors. *J. Electron. Mater.* **51**, 3042 (2022)
 53. C.P. Bean, Magnetization of hard superconductors. *Phys. Rev. Lett.* **8**, 250 (1962)
 54. H. Fallah-Arani, S. Baghshahi, A. Sedghi, N. Riahi-Noori, Enhancement in the performance of BSCCO (Bi-2223) superconductor with functionalized TiO_2 nanorod additive. *Ceram. Int.* **45**, 21878 (2019)
 55. H. Fallah-Arani, S. Baghshahi, A. Sedghi, Impact of functionalized SiC nano-whisker on the flux pinning ability and superconductor features of Bi-2223 ceramics. *Ceram. Int.* **47**, 3706 (2021)
 56. M. Hafiz, R. Abd-Shukor, Effect of Nanosized NiF_2 Addition on the Transport Critical Current Density of Ag-Sheathed $(\text{Bi}_{1.6}\text{Pb}_{0.4})\text{Sr}_2\text{Ca}_2\text{Cu}_3\text{O}_{10}$ superconductor Tapes, *Adv Mater Sci Eng*, **7**, 1 (2015)
 57. N. A.A. Yahya, A. Al-Sharabi, N. R. Mohd Suib, W.S. Chiu, R. Abd-Shukor, Enhanced transport critical current density of (Bi,Pb)-2223/Ag superconductor tapes added with nano-sized Bi_2O_3 , *Ceram. Int.* **42**, 18347 (2016)
 58. R. Griessen et al., Evidence for mean free path fluctuation induced pinning in $\text{YBa}_2\text{Cu}_3\text{O}_7$ and $\text{YBa}_2\text{Cu}_4\text{O}_8$ Films. *Phys. Rev. Lett.* **72**, 1910 (1994)

59. H.H. Wen, Z.X. Zhao, Y.G. Xiao, B. Yin, J.W. Li, Evidence for flux pinning induced by spatial fluctuation of transition temperatures in single domain $(Y_{1-x}Pr_x) Ba_2Cu_3O_{7-\delta}$ samples. *Physica C* **251**, 371 (1995)
60. G. Blatter, M.V. Feigel'man, V.B. Geshkenbein, A.I. Larkin, V.M. Vinokur, Vortices in high-temperature superconductors, *Rev. Mod. Phys.* **66** (1994) 1125
61. H.H. Wen, Z.X. Zhao, R.L. Wang, H.C. Li, B. Yin, Evidence for the lattice-mismatch-stress-field induced flux pinning in $(Gd_{1-x}Y_x) Ba_2Cu_3O_{7-\delta}$ thin films. *Physica C* **262**, 81 (1996)

Publisher's Note Springer Nature remains neutral with regard to jurisdictional claims in published maps and institutional affiliations.

Springer Nature or its licensor (e.g. a society or other partner) holds exclusive rights to this article under a publishing agreement with the author(s) or other rightsholder(s); author self-archiving of the accepted manuscript version of this article is solely governed by the terms of such publishing agreement and applicable law.